Local environments and transport properties of heavily doped strontium barium niobates $Sr_{0.5}Ba_{0.5}Nb_2O_6$.

Riccardo Ottini[†], Cristina Tealdi[‡], Corrado Tomasi[§], Ilenia. G. Tredici[‡], Alessandro Soffientini[‡], Ramón Burriel[¶], Elías Palacios[¶], Miguel Castro Corella[⌘], Umberto Anselmi-Tamburini[‡], Paolo Ghigna[‡], Giorgio Spinolo[‡].

[†] Department of Chemistry, University of Pavia (Italy) [1].

[‡] Department of Chemistry, University of Pavia (Italy) and INSTM – Research Unit at University of Pavia, viale Taramelli 16, I27100 Pavia (Italy).

[§] CNR-ICMATE, UOS Lecco, Corso Promessi Sposi, 29, I23900 Lecco (Italy)

[¶] Instituto de Ciencia de Materiales de Aragón (ICMA) and Departamento de Física de la Materia Condensada, CSIC–Universidad de Zaragoza, Pedro Cerbuna 12, 50009 Zaragoza, Spain

[⌘] Instituto de Ciencia de Materiales de Aragón (ICMA), CSIC–Universidad de Zaragoza, Campus Río Ebro, María de Luna, 3, 50018 Zaragoza, Spain

[1] Now at Dipartimento di Scienze Molecolari e Nanosistemi, University of Venice, Via Torino 155, I 30170 Venezia Mestre (Italy).

ABSTRACT

Strontium barium niobate $Sr_{0.5}Ba_{0.5}Nb_2O_6$ (SBN50) materials have been investigated to explore the effect of heavy doping on the Sr and Nb sites. Un-doped as well as K-doped (40%), Y-doped (40%), Zr-doped (10%), and Mo-doped (12.5%) samples have been characterized for their structural and functional properties (thermo-power, thermal and electrical conductivities) both in the as prepared and reduced states.

For all materials, the EXAFS spectra at the Nb edge can be consistently analyzed with the same model of six shells. In most cases, doping only produces a simple size effect on the structural parameters, while in a few cases doping on the Nb sites weakens the Nb-O bond. Shell sizes and Debye – Waller factors are almost unaffected by temperature and oxidation state, and the disorder is of static nature.

The effects of heavy doping do not agree with a simple model of hole or electron injection by aliovalent substitutions on a large band gap semiconductor.

With respect to the un-doped samples, doping with Mo enhances the thermal conductivity by ~ 50%, Y doping enhances the electrical conductivity by an order of magnitude, while Zr doping increases the Seebeck coefficient by a factor around 2-3. Globally, the ZT efficiency factor of the K-, Y-, and Zr-doped samples is enhanced by one-two orders of magnitude with respect to the un-doped or Mo-doped materials.

INTRODUCTION

With respect to thermo-electric (TE) materials containing elements such as Cd, Tl, Se, Te, Sb, Bi, the oxides of alkali, alkali earth, and transition elements are more health and environmental friendly and the abundance of their constituent elements on Earth's crust is generally orders of magnitude higher. Strontium barium niobates, $Sr_xBa_{1-x}Nb_2O_6$ (SBN), in particular, are interesting because of their low thermal conductivity, which is related to structural features[1,2] such as a basic open network of corner-sharing NbO_6 octahedra, incomplete occupancies of the (Sr, Ba) sites, as well as their nature of solid solutions ($Sr_xBa_{1-x}Nb_2O_6$ x ≈ 0.2 – 0.62 at 1200 °C)[3]. Doping is expected[4,5] to further decrease thermal conductivity, but is mainly investigated in hopes of achieving good values of electrical conductivity (σ) and Seebeck coefficient (S), which are generally too low.

Actually, SBNs have been investigated since long time not only as TE materials[6–12], but also for ferro-electricity[13–21] , dielectric properties[22–25], photocatalysis[26,27], and photorefractive, electro-optic, nonlinear optic, and fluorescence[28–34]. The structural aspects and their effects on the functional properties have been comprehensively discussed by Zhu et al[20] using a crystal-chemical model for the whole family of tetragonal bronzes. Fine details[35–43] of the basic tetragonal tungsten bronze crystal structure[1,2] are affected by Sr/Ba composition, thermal annealing, interaction with external oxygen[44], and the synthetic pathways[10,13–15,17,22–25,36–38,40,41,45–53].

According to literature, the band gap is ca. 3 eV and heavy chemical reduction is required to obtain an *n* - type thermoelectric material from SBNs. The Seebeck coefficient reaches 281 μV/ K at 930 K[7,10] while a three orders of magnitude increase of the electrical conductivity has been

related to a reduction of the binding energy of oxygen vacancies when approaching the ferroelectric transition[11]. The charge transport depends on the reduction temperature and reduction degree, and a polaronic mechanism has been reported by several authors[8,54–56].

Doping of SBN materials at low levels (few %) has been investigated[10,17,24,25,30,37,38,40,41,55,57–64] largely. However, it would be highly desirable to explore the feasibility and effectiveness of doping at high levels, when doping is expected to affect the whole band structure in addition to a simple injection of electrons or holes.

Here, we report the effect on the structure and thermoelectric properties of SNB materials doped with aliovalent cations at high levels. In a previous paper[65] we have shown that a solution chemistry approach is effective in producing SBN materials with nominal 0.5/0.5 (Sr/Ba) composition where 10 - 12.5 % of the Nb sites can be occupied by Zr and Mo, respectively, while the Sr sites can be substituted by K and Y at huge doping levels near 40%. In this paper we analyze the effects of large doping levels on the local structure around Nb and on the transport properties (thermal and electrical conductivities and Seebeck coefficient) of SBN materials-

EXPERIMENTAL

Base-assisted co-precipitation from aqueous solutions of the single cations in the desired stoichiometry was used, followed by an heat treatment at 1150 °C. Details on sample preparation have been reported previously[65].

The X-Ray powder patterns have been taken[65] at room temperature with a Bruker D8 Advance diffractometer equipped with copper anode (Cu-K_α radiation, wavelength = 1.5418 Å) and graphite monochromator on the diffracted beam in the $15° \leq 2\theta \leq 90°$ range with 8 s counting time and 0.02° 2θ steps. For the Rietveld refinements we have used the MAUD program[67] starting from the structure reported by Trubelja et al[2].

XAS spectra have been acquired in transmission mode at the LISA-BM08 beamline[68] (European Synchrotron Radiation Facility, ESRF, Grenoble, Fr) at the Nb–K edge. A Si(311) double crystal has been employed as monochromator and the harmonic rejection has been realized by Pd mirrors, having a cutoff energy of 20 keV. For the measurements, an amount of sample appropriate to give a unit jump in the absorption coefficient at the edge has been weighted, thoroughly mixed with cellulose and pressed to pellet.

The EXAFS has been extracted by using the ATHENA code[69] and the data analysis has been performed using the EXCURVE program[70]. Phases and amplitudes were calculated using the muffin-tin approximation, in the framework of the Hedin–Lundquist and Von Bart approximations for the exchange and ground state potentials, respectively[70]: this includes the effects of inelastic losses due to the electron inelastic scattering (photoelectron mean free path).

To check the reliability of the fits, different weighting schemes have been tested, thus finding that the fitting parameters are recovered within the errors. Multi-channel events are included in the Hedin–Lundquist approximation so that, as expected, we have always found equal to one within the experimental errors the S_0^2 parameter that provides a measure of events like two-electron transitions where the energy difference between the photon and the photoelectron is so large that they are not seen in the spectrum

The fitting model of the EXAFS is based on a simplified radial distribution function around Nb, averaged over the two non-equivalent crystallographic sites of the P4bm tetragonal structure. In particular, the first, second, and third shells are made only of oxygen atoms at distances of about 1.9, 2.0, and 2.1 Å, respectively, in a distorted octahedral coordination. The forth shell, at about 3.4 Å is relative to the A1 sites and contains only Sr, while the fifth shell at a larger distance is relative to the A2 sites; finally a shell at about 3.6 Å from the photo-absorber is due to the Nb atoms in the nearby octahedra. To avoid unnecessary correlation between the fitting parameters, and considering the quite scarce accuracy of EXAFS in the determination of coordination numbers, their values have been kept constant according to the composition of the samples and to the structural information from the scientific literature and from the refinement of powder diffraction data. Then, the shell parameters allowed to vary are only the distance from the photo-absorber and the thermal factor (DW, Debye-Waller). This data analysis strategy is justified by the fact that in all cases, except K that is treated differently, the substituent and substituted ions have the same number of electrons so that the scattering factors are practically indistinguishable. Models with a larger number of shells, up to eight, were tried, but were found unreliable or did not provide meaningful additional information.

Thermal conductivity, κ, was measured by means of a PPMS (Quantum Design) device fitted with a thermal transport option, TTO, on cylindrical samples (8 mm diameter, 2-3 mm thick) with gold plated electrodes stuck by a conductive paste. Heat was applied in order to create a temperature rise of 3% of the basic temperature between the two thermometer shoes . The sample thermal response is dynamically modelled by the TTO system and the thermal conductivity is directly calculated taking into account the applied power, resulting ΔT, and sample geometry. The estimated accuracy is about ± 5%

For the electric transport properties (σ and S) the reduced samples have been used in form of Pt-sputtered cylindrical samples. The electrical conductivity measurements have been obtained with a two-probe cell equipped with Pt electrodes using a MaterialMates mod. 7260 Frequency Response Analyzer. Frequency – independent pure ohmic impedance was always found. The Seebeck coefficient (S) has been determined from the slope of the $\Delta V/\Delta T$ plots using a home-made apparatus. In both cases the measurements have been made under a nitrogen atmosphere to prevent re-oxidation.

RESULTS AND DISCUSSION

Fig. 1 shows the thermal conductivity of SNB materials and its changes with doping. The data are pertinent to reduced samples and already include the electronic contribution, which is almost negligible if appraised with the Widemann - Frantz law. As expected, the un-doped sample shows the highest values. Doping depresses the thermal conductivity, but the trends suggest that above 150 C the Y-, Zr-, and K-doped samples are not very far from the undoped SBN. The Mo-doped sample not only shows the lowest conductivity (about 50% better than the undoped SBN), but also shows lesser temperature dependence than the other dopants.

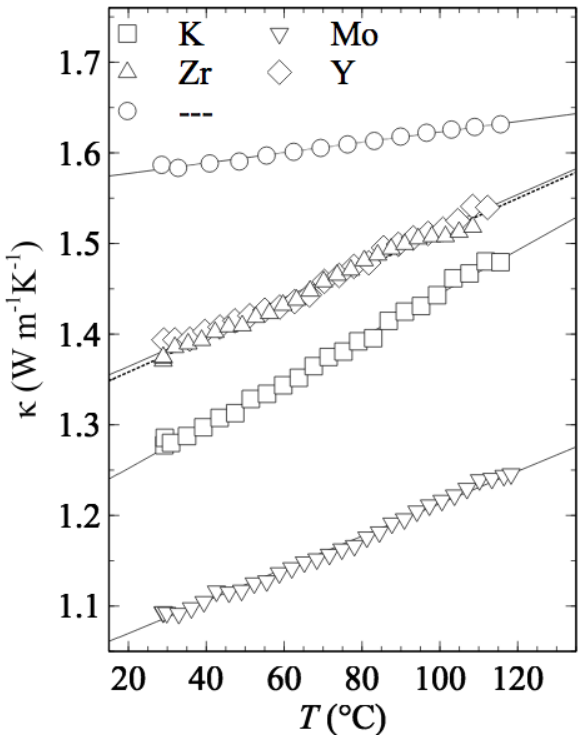

Fig. 1. Thermal conductivity of oxidized SBN materials. The straight lines are linear fits.

The electrical conductivity of reduced samples, as said, is order of magnitude above the values for the oxidized samples. The results (Fig. 2) show that, when reduced under equal conditions, the doped samples generally show conductivity enhancements, but different dopants are very different. With Y, the enhancement amounts to more than one order of magnitude, while Mo

doping is practically ineffective. The conduction mechanism of a non-degenerate semiconductor corresponds to a linear trend in Arrhenius coordinates, but only the Mo and K dopants show a reasonably linear trend (Fig. 3) in the whole temperature range. The deviations from linearity of the other samples are probably due to a transition, with increasing temperature, from a different conduction mechanism.

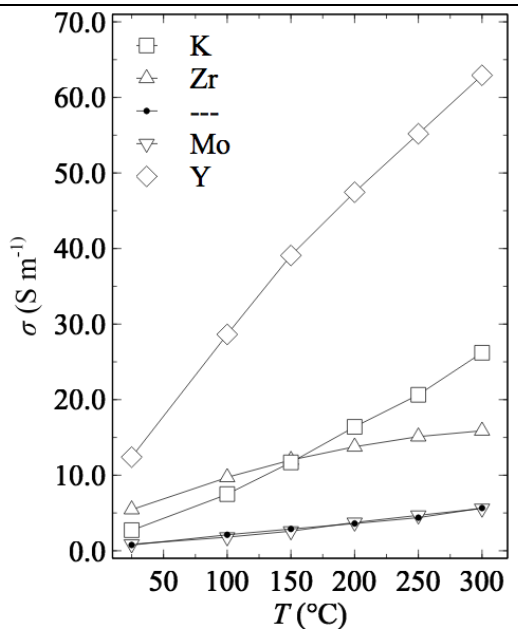

Fig. 2. Electrical conductivity of reduced SBN materials. The lines are guides to eye.

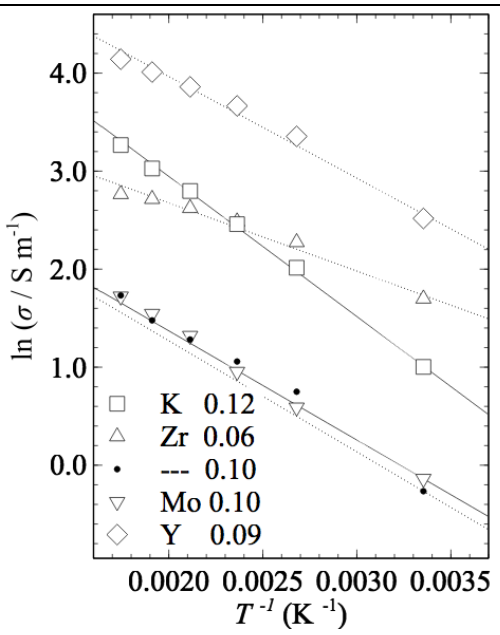

Fig. 3. Arrhenius plots of the data of the previous figure. The numbers are the activation energies of the fits (in eV).

The Seebeck coefficient is always negative and is generally enhanced by doping (Fig. 4). Now, the increase is very small with Mo, better with K and Y, best with Zr, when doping significantly increases also the temperature dependence. With this dopant, starting at around 100 C, the Seebeck coefficient distinctively agrees (Fig. 5) with the model of a non-degenerate semiconductor[9,71,72]:

$$S = \frac{-k_B}{e}\left[ln\frac{N_c}{n} + A\right]; \quad N_c \propto T^{3/2}$$

Also for the Seebeck coefficient, deviation from linearity suggests a possible transition to such behavior with increasing temperature (see Y, in particular).

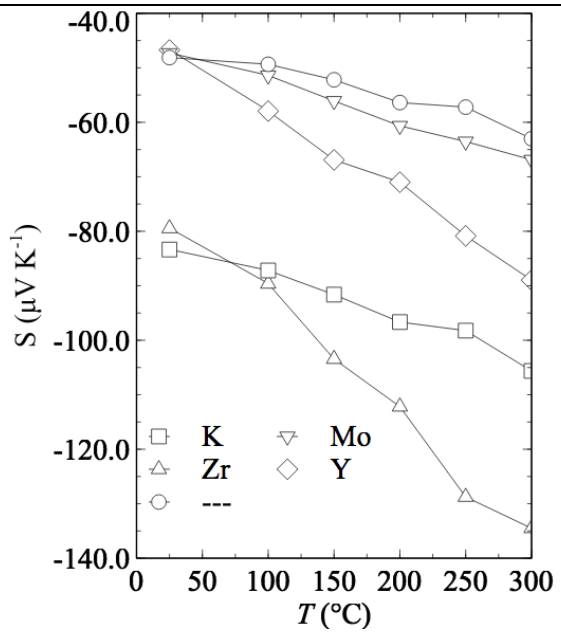

Fig. 4. Seebeck coefficient of reduced SBN materials. The lines are guides to eye.

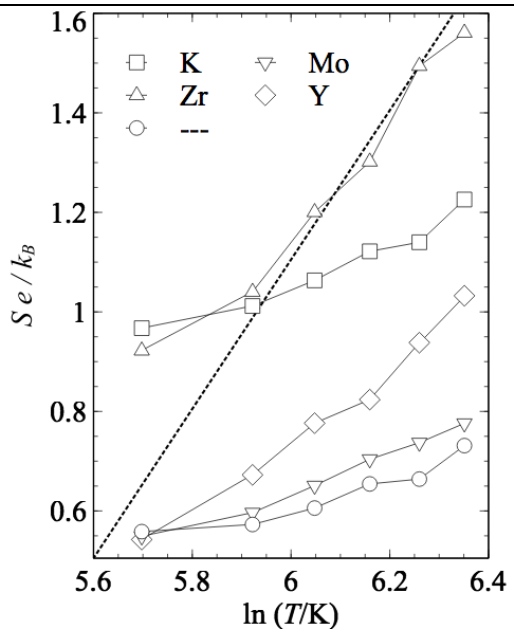

Fig. 5. Seebeck coefficient of reduced SBN materials. The dashed line corresponds to the $S \propto \frac{3}{2}\ln T$ trend.

Let us now discuss the structural changes related to the changes in the functional properties, Strongly simplifying a complex topic, the SBN structure ([1,2]) is based on an open network of corner-sharing NbO_6 octahedra that are arranged in ten rows running along the *c* axis and are connected to each other in one-octahedron-thick layers parallel to the *ab* plane of the tetragonal structure. In the oxygen channels between those rows, there are two main sites (A1 and A2) for the alkali earth cations. Both sites have high (12 and 9, respectively) coordination, fairly large

cation – oxygen distances, and incomplete occupancies. In un-doped SBNs, the A1 sites contain only Sr, while Sr and Ba share the A2 sites, and the amount of Sr lying on A1 or A2 depends on the Sr/Ba ratio. As shown by Fig. 6, doping with ions having different charges and different sizes affects the distribution of the cations.

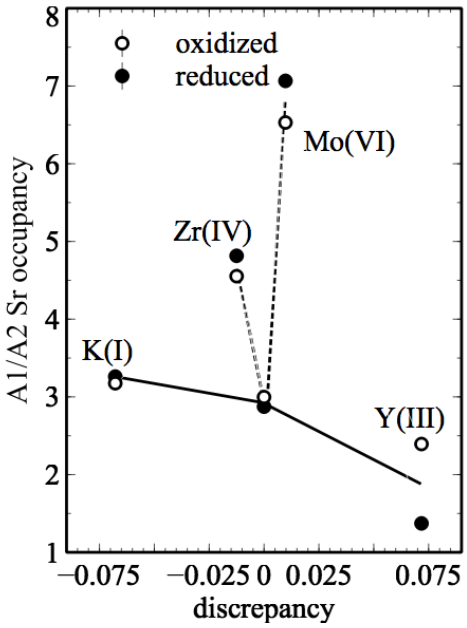

Fig. 6. Sr occupancy ratio of the A1 and A2 sites.

As typically done in solid-state chemistry, the size effect can be discussed using a size discrepancy parameter:

$$\frac{r_0 - r'}{r_0}; \quad r' = x \cdot r + (1 - x) \cdot r_0$$

where x is the mole fraction of the dopant, r_0 is the size of the replaced ion, while r is the size of the replacing ion[73]. The A1/A2 occupancy ratio of Sr (Fig. 6) appears related to the discrepancy parameter in two clearly different ways. For K and Y (the dopants replacing Sr) there is an almost linear trend that interpolates close to the value of the un-doped sample. Instead, doping on the Nb sites increases the occupancy of the A1 sites independently both of size and charge state of

the replacing ion.

The local structure around Nb has been investigated with EXAFS at the Nb-K edge. Fig. 7 shows an example of the EXAFS signal with the fit according to the six shells model, as described in the experimental section. The peaks in the FT (Fourier transform, right part) show that the cation shells (next nearest shells) affect the EXAFS only above 3 Å.

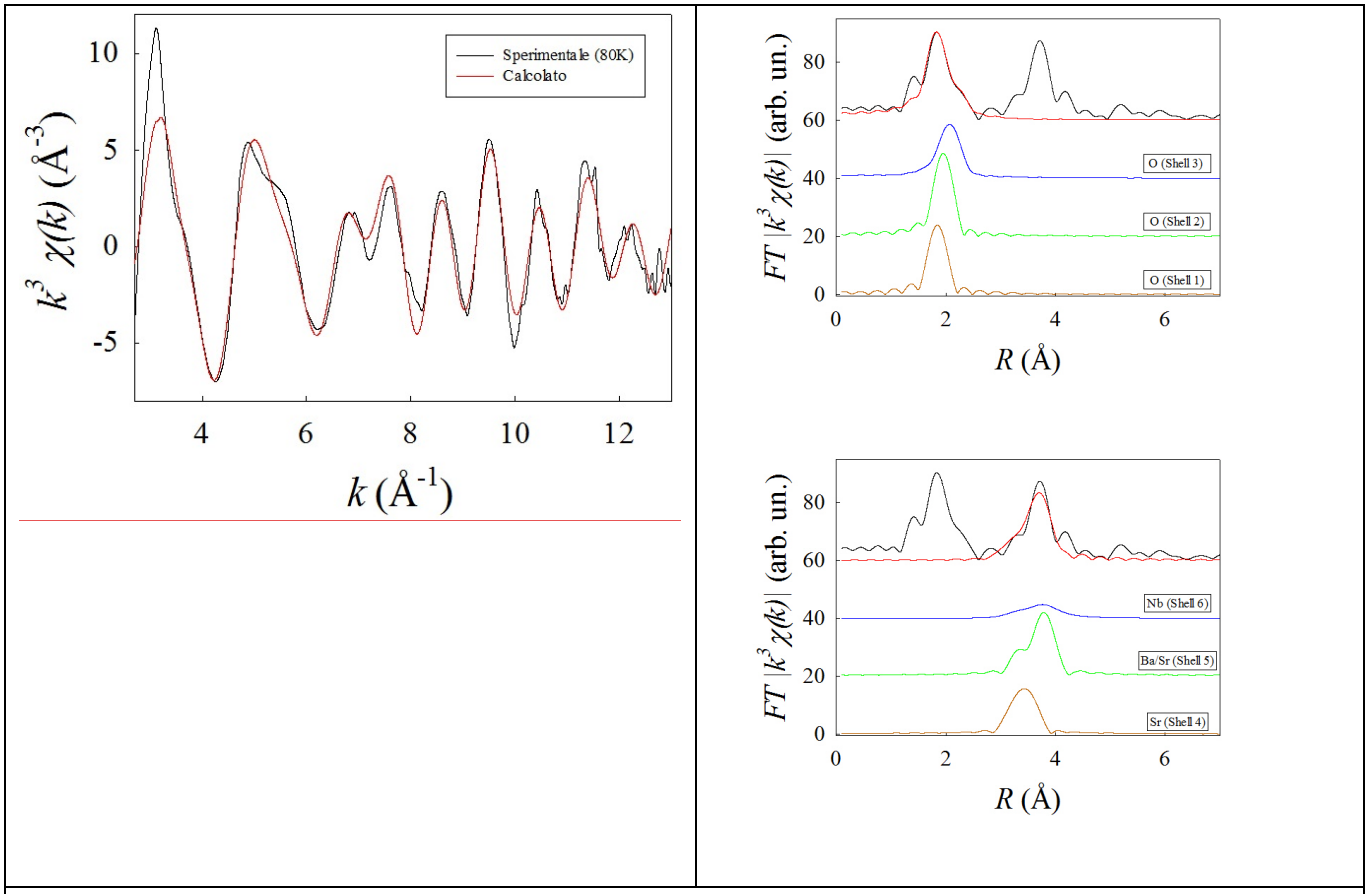

Fig. 7. EXAFS of the un-doped oxidized sample at 80 K (left part) and (right part) its Fourier transform with the components due (upper panel) to the first, second and third Nb-O shells and (lower panel part) to the Nb-A1, Nb-A2 and Nb-Nb shells.

The local environments of the Nb sites can be consistently analyzed with these shells, independently of temperature, nature of the dopant and oxidation state of the sample.

The nature of the dopant generally affects the shell parameters in two clearly different ways: a) for some parameters there is a regular and roughly linear trend with the size discrepancy factor, b) for other parameters a linear trend can be found with substitutions on the A sites, but substitutions on the Nb sites produce shifts of the same sign with respect to the un-doped sample. The first behavior is reasonably indicative of a simple ion size effect and concerns the *c* lattice constant[65] and all shell sizes (Fig. 8). Going from K to Y, the changes of the respective parameters amount to a few %: 1.5 – 5% depending on the parameter. A similar trend can be seen also for the DW factors of the third oxygen shell and the Nb-A1 and Nb-A2 shells. The second behavior is indicative of a weakening of the Nb – O bonds and concerns the *a* lattice constant[65] as well as the A1/A2 occupancy ratio (Fig. 6).

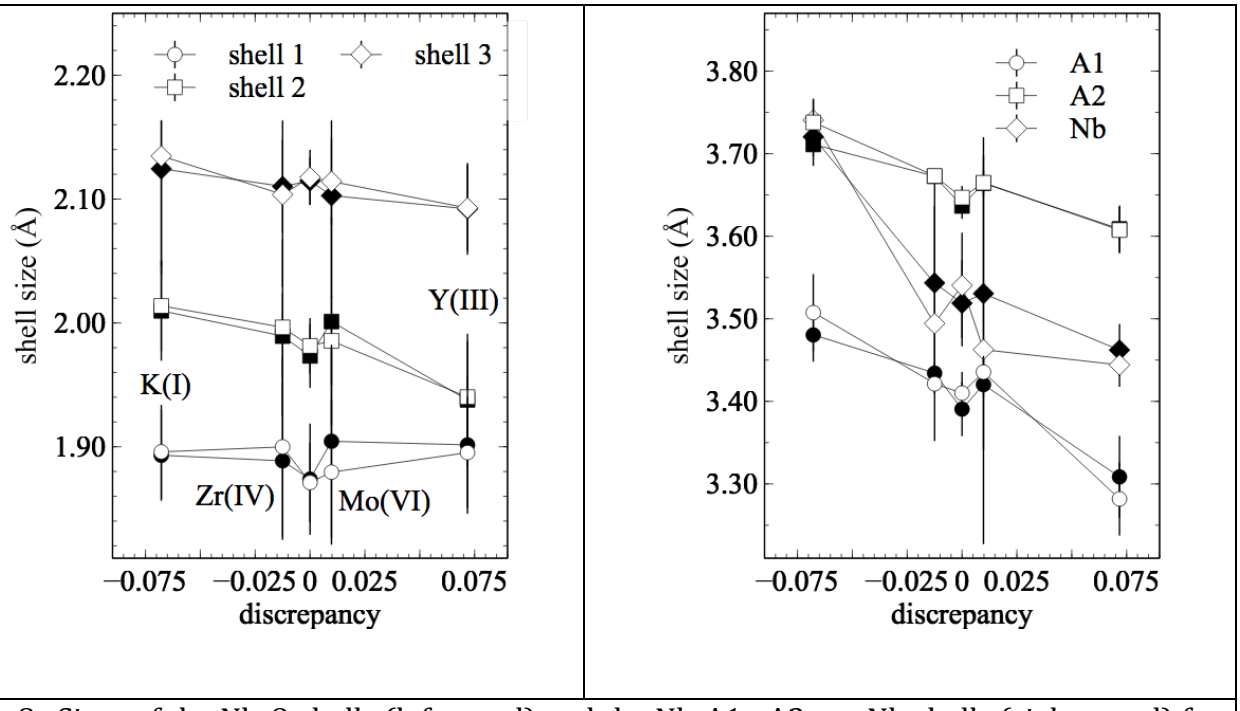

Fig. 8. Sizes of the Nb-O shells (left panel) and the Nb-A1, -A2 or –Nb shells (right panel) for various dopants at 80 K. Open and filled symbols refer to oxidized and reduced samples.

Almost generally, temperature does not significantly affect shell sizes and DW factors: examples are given in Fig. 9. Static disorder always predominates over thermal disorder, a result that is in

full agreement with the very low experimental values of the thermal conductivity and can be related to the general features of the structure, but we warn that the result can be due also to the data analysis procedure that groups various sub-shells into fewer composite shells.

Finally, the oxidation state of the sample does not generally affect in a significant way the structural parameters, lattice constants, A1/A2 occupancy, sizes, and DW factors of the various shells.

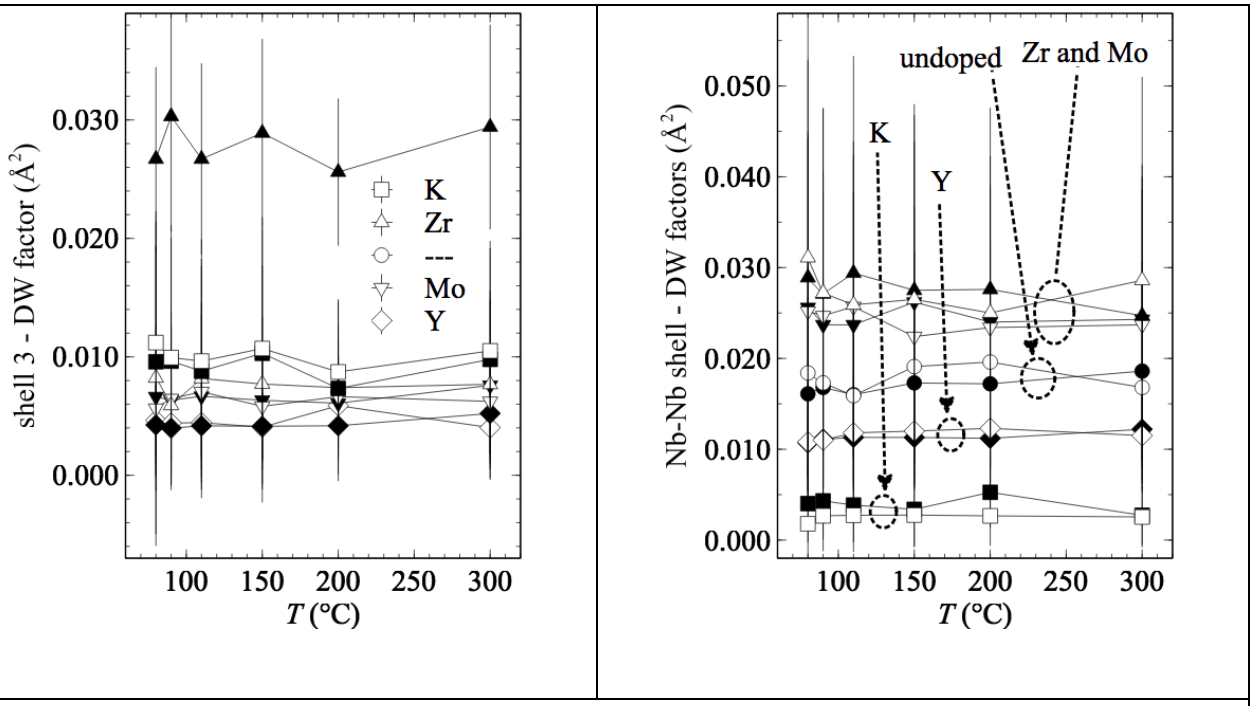

Fig. 9. Trend with temperature of the DW factors of the third Nb-O shell (left panel) and the Nb-Nb shell (right panel). Open and filled symbols refer to oxidized and reduced samples.

There are few exceptions to these general trends.

a) A small and not fully reliable hint of thermal disorder can be seen on the DW factors of the Nb-A1 and Nb-A2 shells of un-doped, Zr-doped, or Mo-doped samples.

b) Differently from the other dopants and from the undoped case, the K-doped samples show a) Nb-A2 and Nb-Nb shell sizes practically equal to each other (right panel of Fig. 8), while all the

DW factors of all the Nb-cation shells (see right panel of Fig. 9 for an example) are zero to within the experimental errors. All these features are unaffected by changes of temperature and oxidation state. A reasonable explanation relies in the large size of the K^+ ion: the A2 site is where K replaces Sr. We understand that K strains the structure much more than the other dopants and gives rise to a stronger correlation between the displacements of Nb and the ions in the A2 site.

c) There is a strong effect of chemical reduction on the DW factor of the third Nb-O shell for the Zr-doped sample. The effect can be seen in all the temperature range (left panel of Fig. 10).

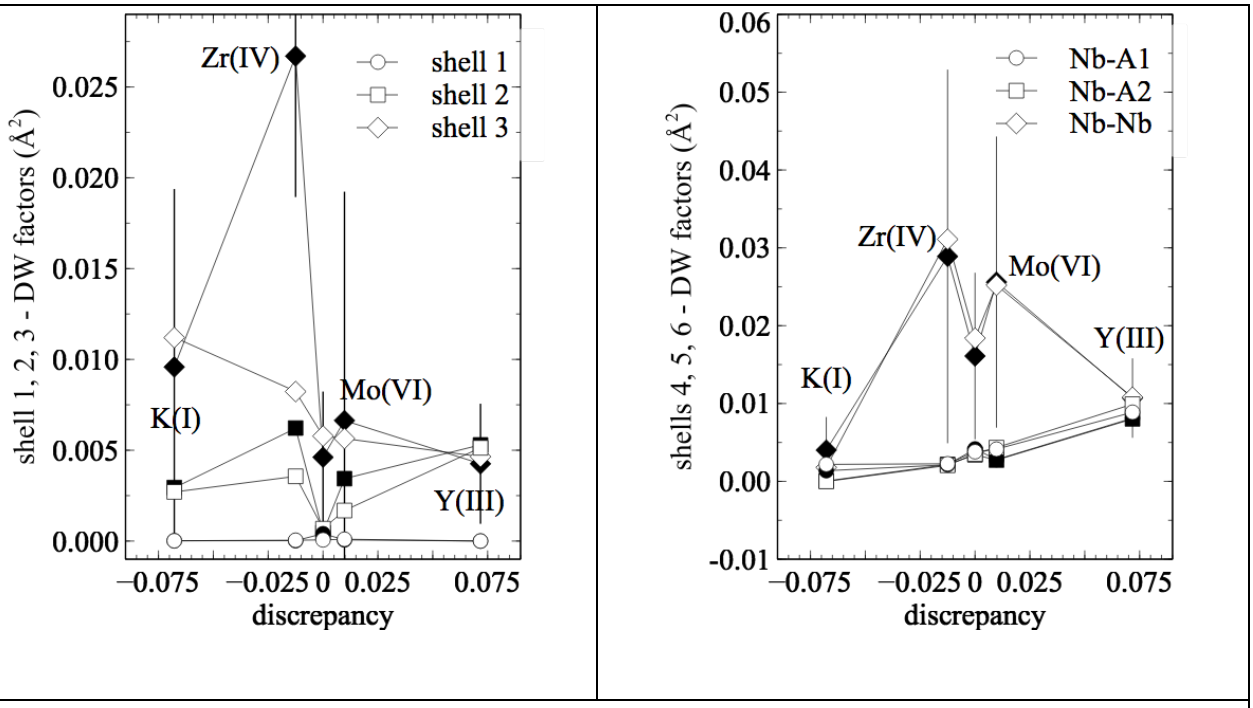

Fig. 10. DW factors of various shells for various dopants at 80 K. Open and filled symbols refer to oxidized and reduced samples. For better clarity, in the right panel the error bars o are shown only for the Nb-Nb shell of the reduced sample

d) The DW factors of the Nb-Nb shell (right panel of Fig. 9) depend on nature of the dopant in a distinctive way, as doping on the Sr sites both with K and Y reduces the DW factors with respect to the undoped samples. Incidentally, also the dopants on the Nb sites affect the DW factors in the same direction, which is now an increase of the value, but the latter trend is typical of other structural parameters, as said.

Conclusions

The modification of the band structure and the possibility of injecting mobile carriers with huge doping of the SNB structure can be discussed making reference to a simple two-bands model and two mechanisms. The first one is the direct compensation of the charged substitutional defects with free electrons or holes. Writing the reactions with a doping oxide entering and a regular oxide leaving the structure just to keep simple the notation, these are:

$$K_2O + 2\,Sr_{Sr}^{x} + \tfrac{1}{2}\,O_2(gas) \longrightarrow 2\,K'_{Sr} + 2\,h^{\bullet} + 2\,SrO$$

$$Y_2O_3 + 2\,Sr_{Sr}^{x} \longrightarrow 2\,Y_{Sr}^{\bullet} + 2\,e' + \tfrac{1}{2}\,O_2(gas) + 2\,SrO$$

$$2\,ZrO_2 + 2\,Nb_{Nb}^{x} + \tfrac{1}{2}\,O_2(gas) \longrightarrow 2\,Zr'_{Nb} + 2\,h^{\bullet} + Nb_2O_5$$

$$2\,MoO_3 + 2\,Nb_{Nb}^{x} \longrightarrow 2\,Mo_{Nb}^{\bullet} + \tfrac{1}{2}\,O_2(gas) + 2\,e' + Nb_2O_5$$

With the other mechanism, the substitutional defects are balanced by oxygen defects that in turn produce the mobile carriers with a successive interaction with the external atmosphere. For doping on the Sr sites this is:

$$K_2O + 2\,Sr_{Sr}^{x} \longrightarrow 2\,K'_{Sr} + V_O^{\bullet\bullet} + 2\,SrO \quad \text{followed by} \quad V_O^{\bullet\bullet} + \tfrac{1}{2}\,O_2(gas) \rightleftarrows O_O^{x} + 2\,h^{\bullet} \text{ or}$$

$$Y_2O_3 + 2\,Sr_{Sr}^{x} \longrightarrow 2\,Y_{Sr}^{\bullet} + O_i'' + + 2\,SrO \quad \text{followed by} \quad O_i'' \rightleftarrows \tfrac{1}{2}\,O_2(gas) + 2\,e'$$

Doping on the Nb sites can be treated in a closely similar way. According to both these mechanisms, doping with lower valence or higher valence cations should produce opposite effects for what concerns the sign of the injected carriers and the need of a reduction or oxidation step, respectively, to produce the mobile carriers. This simple scheme also suggests the appealing possibility of achieving both *n*-type and *p*-type SBN conductors using different dopants, and

achieving performing *n*-type conductors without high temperature treatments under low oxygen partial pressures.

The most striking result of the present investigation of heavy doping of the SNB structure is that the actual effects of doping are remarkably different from all these naïve expectations.

Aliovalent dopants of opposite charges do not show opposite effects on many aspects and in particular on carrier injection. By itself, doping produces only insulating materials, reduction is always required to produce electrically conductive materials, and these become *n*-type conductors both with a higher or lower valence.

Even when pushed to 10-12 % of the Nb sites or a huge 40% of the Sr sites, doping does not produce significant modifications of the SNB structure and enhancements of its TE properties by orders of magnitude.

As previously discussed[65], there is a negligible effect of doping also concerning the charge state of Nb, which remains V irrespective of nature of dopant, temperature and redox treatment. We also found that fine differences in intensity of a pre-edge feature of the XAS spectrum indicate that doping affects the density of empty Nb 4d states. Also results is in disagreement with the simple picture of aliovalent doping: a higher-valence cation should increase the spectral weight while a lower-valence cation is expected to decrease the spectral weight while, experimentally, the K and Mo doped samples are similar to the un-doped sample, the Y-doped sample shows higher intensity, and the Zr-doped sample shows lower intensity. We incidentally remind (see above) that the Zr doped sample is particular in showing a clear structural effect of chemical reduction, i.e. a particularly large DW factor of its 3rd Nb-O shell in all temperature range.

Most of the structural parameters change with nature of the dopant in a way that is directly explained by a simple ion size effect. The different trends of the *a* lattice constant[65] and the A1/A2 occupancy ratio are indicative of a weakening of the Nb – O bonds and again do not show opposite effects when the sign of the substitutional defect is changed.

With a single exception for the DW factor of the third Nb-O shell of the Zr-doped sample, the structural parameters do not show remarkable effects of chemical reduction.

The O shells do not generally show marked difference with nature of dopant, which seems to suggest that the substitutional defects are not stoichiometrically compensated by oxygen defects.

A reasonable explanation of these aspects is that the substitutional defects give rise to shallow levels and are therefore unable to inject mobile carriers either directly or through oxygen defects. Huge jumps of electrical conductivity are obtained by chemical reduction of the different samples under similar conditions: this indicates that the onset of conductivity is entirely due to oxygen vacancies that form under low oxygen partial pressure while place, size and charge of the dopants seemingly play a minor role.

While huge doping with aliovalent cations does not allow the desired improvements of the basic strategy towards preforming TE materials of the SBN family, it is anyway able to produce enhancements of the order of a power of ten.

The smallest effect is on the thermal conductivity: all dopants decrease the property but the change is at most 25 % (with Mo-doping) and around 10% or below for the other dopants.

Mo doping does not affect significantly the electrical conductivity of the reduced samples, while the other dopants produce an increase of 10 times (Y) or 3-5 times (K and Zr).

The Seebeck coefficient is always negative and enhanced by doping. The increase is very small with Mo, better with K and Y, best with Zr, when doping significantly increases also the temperature dependence.

Finally, the power factor is clearly better (one order of magnitude) for Y -, K –, and Zr doped samples and this trend is closely followed by the ZT coefficientFinally, the power factor and the ZT (Fig. 1).

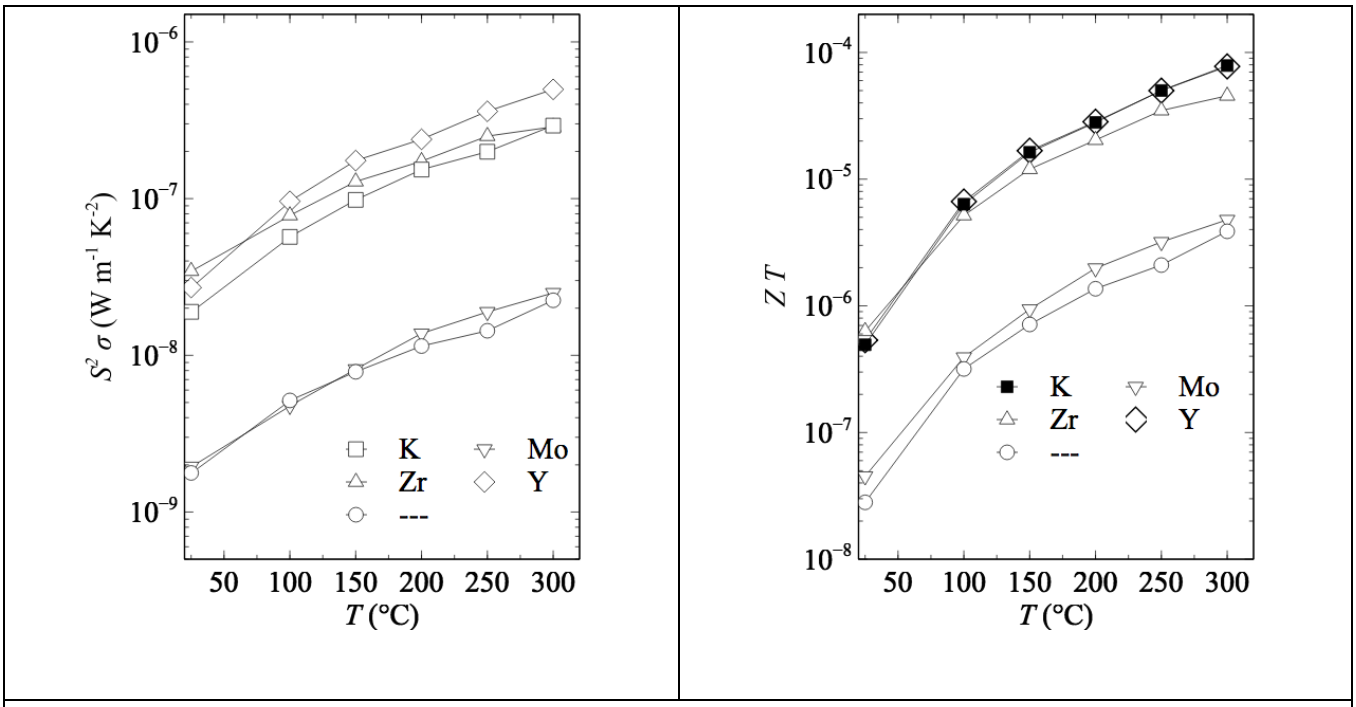

Fig. 11. Effect of doping on power factor (left) and the *ZT* thermoelectric efficiency parameter (right) of the various samples after reduction.

ACKNOWLEDGMENTS

This work has been supported by the "Materiali Avanzati" Program (Projet code 2012-0815) of the Cariplo foundation (Milano, Italy). BM08 (LISA)@ESRF is acknowledged for the provision of beam-time, travel and accommodation expenses (Exp. HC-1582). Thanks are given to Dr Francesco d'Acapito for considerable help during experiment setup and data collection.

REFERENCES

(1) Jamieson, P. B.; Abrahams, S. C.; Bernstein, J. L. Ferroelectric Tungsten Bronze-Type Crystal Structures. I. Barium Strontium Niobate $Ba_{0.27}Sr_{0.75}Nb_2O_{5.78}$. *The Journal of Chemical Physics* **1968**, *48* (11), 5048–5057.

(2) Trubelja, M. P.; Ryba, E.; Smith, D. K. A Study of Positional Disorder in Strontium Barium Niobate. *J. Mater. Sci.* **1996**, *31* (6), 1435–1443.

(3) Nikasch, C.; Göbbels, M. Phase Relations and Lattice Parameters in the System SrO–BaO–Nb_2O_5 Focusing on SBN ($Sr_xBa_{1-x}Nb_2O_6$). *Journal of Crystal Growth* **2004**, *269* (2–4), 324–332.

(4) Slack, G. A. New Materials and Performance Limits for Thermoelectric Cooling. In *CRC Handbook of Thermoelectrics*; CRC Press, 1995; pp 407–440.

(5) Tritt, T. M. Thermoelectric Phenomena, Materials, and Applications. In *Annual review of materials research*; Annual Review of Materials Research; Annual Reviews, 2011; Vol. 41, pp 433–448.

(6) Wagner, K.; Hegenbarth, E. Thermal-Conductivity of Strontium-Barium-Niobat Under High-Pressure And. *Ferroelectr. Lett. Sect.* **1993**, *16* (3-4), 95–102.

(7) Lee, S.; Wilke, R. H. T.; Trolier-McKinstry, S.; Zhang, S.; Randall, C. A. $Sr_xBa_{1-x}Nb_2O_{6-\delta}$ Ferroelectric-Thermoelectrics: Crystal Anisotropy, Conduction Mechanism, and Power Factor. *Appl. Phys. Lett.* **2010**, *96* (3), 031910.

(8) Lee, S.; Dursun, S.; Duran, C.; Randall, C. A. Thermoelectric Power Factor Enhancement of Textured Ferroelectric $Sr_xBa_{1-x}Nb_2O_{6-\delta}$ Ceramics. *Journal of Materials Research* **2011**, *null* (01), 26–30.

(9) Lee, S.; Bock, J. A.; Trolier-McKinstry, S.; Randall, C. A. Ferroelectric-Thermoelectricity and Mott Transition of Ferroelectric Oxides with High Electronic Conductivity. *Journal of the European Ceramic Society* **2012**, *32* (16), 3971–3988.

(10) Dandeneau, C. S.; Bodick, T. W.; Bordia, R. K.; Ohuchi, F. S. Thermoelectric Properties of Reduced Polycrystalline $Sr_{0.50}Ba_{0.50}Nb_2O_6$ Fabricated Via Solution Combustion Synthesis. *J. Am. Ceram. Soc.* **2013**, *96* (7), 2230–2237.

(11) Mahan, G. D.; Sofo, J. O. The Electrical Conductivity of Strontium-Barium Niobate. *J. Electron. Mater.* **2013**, *42* (7), 1375–1376.

(12) Choy, C. L.; Leung, W. P.; Xi, T. G.; Fei, Y.; Shao, C. F. Specific Heat and Thermal Diffusivity of Strontium Barium Niobate ($Sr_{1-x}Ba_xNb_2O_6$) Single Crystals. *Journal of Applied Physics* **1992**, *71* (1), 170–173.

(13) Yang, Y. S.; Ryu, M. K.; Joo, H. J.; Lee, S. H.; Lee, S. J.; Kang, K. Y.; Jang, M. S. Ferroelectricity and Electronic Defect Characteristics of *c*-Oriented $Sr_{0.25}Ba_{0.75}Nb_2O_6$ Thin Films Deposited on Si Substrates. *Appl. Phys. Lett.* **2000**, *76* (23), 3472–3474.

(14) Liu, S. T.; Maciolek, R. B. Rare-Earth-Modified $Sr_{0.5}Ba_{0.5}Nb_2O_6$ Ferroelectric Crystals and

Their Applications as Infrared Detectors. *JEM* **1975**, *4* (1), 91–100.

(15) Mattausch, G.; Felsner, T.; Hegenbarth, E.; Kluge, B.; Sahling, S. Glassy Properties of the Relaxor Ferroelectric Strontium Barium Niobate at Low Temperatures. *Phase Transit.* **1996**, *59* (4), 189–223.

(16) Murty, S.; Murthy, K.; Padmavathi, G.; Bhanumathi, A.; Murty, K. *Relaxor Studies of Na, Fe and Mg Doped Sbn Ceramics*; Liu, M., Safari, A., Kingon, A., Haertling, G., Eds.; I E E E: New York, 1992.

(17) Bhaumik, I.; Ganesamoorthy, S.; Bhatt, R.; Subramanian, N.; Karnal, A. K.; Gupta, P. K.; Takekawa, S.; Kitamura, K. Influence of Cerium Doping on the Dielectric Relaxation of $Sr_{0.75}Ba_{0.25}Nb_2O_6$ Single Crystal Grown by the Double Crucible Stepanov Technique. *J. Alloy. Compd.* **2015**, *621*, 26–29.

(18) Kshirsagar, S. H.; Jigajeni, S. R.; Tarale, A. N.; Salunkhe, D. J.; Joshi, P. B. Investigations on Fe-Doped Strontium Barium Niobate, Single Phase Ferroelectric and Magnetodielectric Compounds. *J. Adv. Dielectr.* **2015**, *5* (1), 1550001.

(19) Dudhe, C. M.; Nagdeote, S. B.; Chaudhari, C. P. Ferroelectric Domains in Sr0.5Ba0.5Nb2O6 (SBN50) at Nanolevel. *Ferroelectrics* **2015**, *482* (1), 104–112.

(20) Zhu, X.; Fu, M.; Stennett, M. C.; Vilarinho, P. M.; Levin, I.; Randall, C. A.; Gardner, J.; Morrison, F. D.; Reaney, I. M. A Crystal-Chemical Framework for Relaxor versus Normal Ferroelectric Behavior in Tetragonal Tungsten Bronzes. *Chem. Mat.* **2015**, *27* (9), 3250–3261.

(21) Olsen, G. H.; Aschauer, U.; Spaldin, N. A.; Selbach, S. M.; Grande, T. Origin of Ferroelectric Polarization in Tetragonal Tungsten-Bronze-Type Oxides. *Phys. Rev. B* **2016**, *93* (18), 180101.

(22) Liu, Y.; Ong, C. W.; Choy, C. L.; Chan, P. W. Dielectric and Ferroelectric Properties of Pulsed Laser Deposited Strontium Barium Niobate Thin Films. In *Ferroelectric Thin Films V*; Desu, S. B., Ramesh, R., Tuttle, B. A., Jones, R. E., Yoo, I. K., Eds.; Materials Research Soc: Pittsburgh, 1996; Vol. 433, pp 131–136.

(23) Chen, G.; Qi, B. Microstructure and Dielectric Properties of CBS Glass-Doped $Sr_{0.5}Ba_{0.5}Nb_2O_6$ Ceramic System. *J. Mater. Sci.-Mater. Electron.* **2009**, *20* (3), 248–252.

(24) Stanciu, G.; Achim, A.; Scarisoreanu, N. D.; Ion, V.; Birjega, R.; Andronescu, E.; Dinescu, M. Synthesis of Calcium Doped Strontium Barium Niobate Ceramic Samples. *Optoelectron. Adv. Mater.-Rapid Commun.* **2015**, *9* (5-6), 720–723.

(25) Velayutham, T. S.; Salim, N. I. F.; Gan, W. C.; Abd. Majid, W. H. Effect of Cerium Addition on the Microstructure, Electrical and Relaxor Behavior of Sr0.5Ba0.5Nb2O6 Ceramics. *Journal of Alloys and Compounds* **2016**, *666*, 334–340.

(26) Fan, D.; Chong, R.; Fan, F.; Wang, X.; Li, C.; Feng, Z. A Tetragonal Tungsten Bronze-Type Photocatalyst: Ferro-Paraelectric Phase Transition and Photocatalysis. *Chin. J. Catal.* **2016**, *37* (8), 1257–1262.

(27) Fan, D.; Zhu, J.; Wang, X.; Wang, S.; Liu, Y.; Chen, R.; Feng, Z.; Fan, F.; Li, C. Dual Extraction of Photogenerated Electrons and Holes from a Ferroelectric Sr0.5Ba0.5Nb2O6 Semiconductor. *ACS Appl. Mater. Interfaces* **2016**, *8* (22), 13857–13864.

(28) Sakamoto, S.; Yazaki, T. Anomalous Electro-optic Properties of Ferroelectric Strontium Barium Niobate and Their Device Applications. *Appl. Phys. Lett.* **1973**, *22* (9), 429–431.

(29) Ewbank, M.; Neurgaonkar, R.; Cory, W.; Feinberg, J. Photorefractive Properties of Strontium-

Barium Niobate. *J. Appl. Phys.* **1987**, *62* (2), 374–380.

(30) Baetzold, R. Calculations of Defect Properties Important in Photorefractive $Sr_{0.6}Ba_{0.4}Nb_2O_6$. *Phys. Rev. B* **1993**, *48* (9), 5789–5796.

(31) Kume, T.; Nonaka, K.; Yamamoto, M. Wavelength-Multiplexed Holographic Recording in Cerium Doped Strontium Barium Niobate by Using Tunable Laser Diode. *Jpn. J. Appl. Phys.* **1996**, *35* (1B), 448–453.

(32) Daldosso, M.; Speghini, A.; Ghigna, P.; Ramirez, M. de la O.; Jaque, D.; Bausa, L. E.; Sole, J. G.; Bettinelli, M. Lanthanide Doped Strontium Barium Niobate: Optical Spectroscopy and Local Structure at the Impurity Sites. *J. Alloy. Compd.* **2008**, *451* (1-2), 12–17.

(33) Molina, P.; Loro, H.; Alvarez-Garcia, S.; Bausa, L. E.; Martin Rodriguez, E.; Guillot-Noel, O.; Goldner, P.; Bettinelli, M.; Ghigna, P.; Garcia Sole, J. Site Location and Crystal Field of Nd^{3+} Ions in Congruent Strontium Barium Niobate. *Phys. Rev. B* **2009**, *80* (5), 054111.

(34) Zhou, Y. Correlated Oxides: Material Physics and Devices. Doctoral Dissertation, Harvard University, 2015.

(35) Chernaya, T. S.; Maksimov, B. A.; Verin, I. V.; Ivleva, L. I.; Simonov, V. I. Crystal Structure of $Ba_{0.39}Sr_{0.61}Nb_2O_{5.78}$ Single Crystals. *Crystallogr. Rep.* **1997**, *42* (3), 375–380.

(36) Chernaya, T. S.; Maksimov, B. A.; Verin, I. A.; Ivleva, L. I.; Simonov, V. I. Refinement of the Single-Crystal Structure of $Sr_{0.61}Ba_{0.39}Nb_2O_6$: Ce. *Crystallogr. Rep.* **1998**, *43* (6), 986–990.

(37) Chernaya, T. S.; Maksimov, B. A.; Volk, T. R.; Ivleva, L. I.; Simonov, V. I. Atomic Structure of $Sr_{0.75}Ba_{0.25}Nb_2O_6$ Single Crystal and Composition-Structure-Property Relation in $(Sr,Ba)Nb_2O_6$ Solid Solutions. *Phys. Solid State* **2000**, *42* (9), 1716–1721.

(38) Chernaya, T. S.; Volk, T. R.; Maksimov, B. A.; Blomberg, M. K.; Ivleva, L. I.; Verin, I. A.; Simonov, V. I. X-Ray Diffraction Study of Cerium-and Thulium-Doped (Sr,Ba)Nb_2O_6 Single Crystals. *Crystallogr. Rep.* **2003**, *48* (6), 933–938.

(39) Schefer, J.; Schaniel, D.; Petricek, V.; Woike, T.; Cousson, A.; Woehlecke, M. Reducing the Positional Modulation of NbO(6)-Octahedra in Sr(x)Ba(1-x)Nb(2)O(6) by Increasing the Barium Content: A Single Crystal Neutron Diffraction Study at Ambient Temperature for x=0.61 and x=0.34. *Z. Kristall.* **2008**, *223* (6), 399–407.

(40) Kuz'micheva, G. M.; Ivleva, L. I.; Kaurova, I. A.; Rybakov, V. B. Structural Peculiarities and Point Defects of Undoped and Cr- and Ni-Doped $Sr_{0.61}Ba_{0.39}Nb_2O_6$ Crystals. *Acta Mater.* **2014**, *70*, 208–217.

(41) Kaurova, I. A.; Kuz'micheva, G. M.; Ivleva, L. I.; Chernyshev, V. V.; Rybakov, V. B.; Domoroshchina, E. N. X-Ray Powder Diffraction Methods for the Determination of Composition and Structural Parameters of Cr- and Ni-Doped $Sr_{0.61}Ba_{0.39}Nb_2O_6$ Crystals. *J. Alloy. Compd.* **2015**, *638*, 159–165.

(42) Chillal, S.; Koulialias, D.; Gvasaliya, S. N.; Cowley, R. A.; Ivleva, L. I.; Lushnikov, S. G.; Zheludev, A. Phase Transition of Chemically Doped Uniaxial Relaxor Ferroelectric. *J. Phys.-Condes. Matter* **2015**, *27* (43), 435901.

(43) Gvasaliya, S. N.; Cowley, R. A.; Ivleva, L. I.; Lushnikov, S. G.; Roessli, B.; Zheludev, A. Phase Transition of the Uniaxial Disordered Ferroelectric Sr0.61Ba0.39Nb2O6. *J. Phys.-Condes. Matter* **2014**, *26* (18), 185901.

(44) Bock, J. A.; Chan, J. H.; Tsur, Y.; Trolier-McKinstry, S.; Randall, C. A. The Effects of Low

Oxygen Activity Conditions on the Phase Equilibria and Cation Occupancy of Strontium Barium Niobate. *J. Am. Ceram. Soc.* **2016**, *99* (10), 3435–3442.

(45) Chernaya, T. S.; Volk, T. R.; Verin, I. A.; Ivleva, L. I.; Simonov, V. I. Atomic Structure of $(Sr_{0.50}Ba_{0.50})Nb_2O_6$ Single Crystals in the Series of $(Sr_xBa_{1-X})Nb_2O_6$ Compounds. *Crystallogr. Rep.* **2002**, *47* (2), 213–216.

(46) Gao, M.; Kapphan, S.; Porcher, S.; Pankrath, R. Experimental Study of NIR Absorption due to Nb^{4+} Polarons in Pure and Cr- or Ce-Doped SBN Crystals. *J. Phys.-Condes. Matter* **1999**, *11* (25), 4913–4924.

(47) Melo, M.; Araujo, E. B.; Turygin, A. P.; Shur, V. Y.; Kholkin, A. L. Physical Properties of Strontium Barium Niobate Thin Films Prepared by Polymeric Chemical Method. *Ferroelectrics* **2016**, *496* (1), 177–186.

(48) Said, M.; Velayutham, T. S.; Gan, W. C.; Abd Majid, W. H. The Structural and Electrical Properties of $Sr_xBa_{(1-x)}Nb_2O_6$ (SBN) Ceramic with Varied Composition. *Ceram. Int.* **2015**, *41* (5), 7119–7124.

(49) Patro, P. K.; Kulkarni, A. R.; Harendranath, C. S. Dielectric and Ferroelectric Behavior of SBN50 Synthesized by Solid-State Route Using Different Precursors. *Ceram. Int.* **2004**, *30* (7), 1405–1409.

(50) Hirano, S.; Yogo, T.; Kikuta, K.; Ogiso, K. Preparation of Strontium Barium Niobate by Sol-Gel Method. *J. Am. Ceram. Soc.* **1992**, *75* (6), 1697–1700.

(51) Tanaka, S.; Takahashi, T.; Uematsu, K. Fabrication of Transparent Crystal-Oriented Polycrystalline Strontium Barium Niobate Ceramics for Electro-Optical Application. *J. Eur. Ceram.*

Soc. **2014**, *34* (15), 3723–3728.

(52) Ebina, Y.; Higuchi, T.; Hattori, T.; Tsukamoto, T. *Electronic Structure in the Valence Band of* c-*Axis Oriented* $Sr_{0.50}Ba_{0.50}Nb_2O_6$ *Thin Film on* $La_{0.05}Sr_{0.95}TiO_3$ *Substrate*; Somiya, S., Doyama, M., Eds.; Elsevier Science Bv: Amsterdam, 2006; Vol. 31.

(53) Podlozhenov, S.; Graetsch, H. A.; Schneider, J.; Ulex, M.; Woehlecke, M.; Betzler, K. Structure of Strontium Barium Niobate $Sr_xBa_{1-x}Nb_2O_6$ (SBN) in the Composition Range 0.32 <= X <= 0.82. *Acta Crystallogr. Sect. B-Struct. Sci.* **2006**, *62*, 960–965.

(54) Dandeneau, C. S.; Yang, Y.; Olmstead, M. A.; Bordia, R. K.; Ohuchi, F. S. Polaronic Conduction and Anderson Localization in Reduced Strontium Barium Niobate. *Appl. Phys. Lett.* **2015**, *107* (23), 232901.

(55) Demirbilek, R.; Kutsenko, A. B.; Pankrath, R.; Kapphan, S. E. Absorption Spectroscopy and Energy Levels of Rare Earth Impurity Centres in $Sr_xBa_{1-x}Nb_2O_6$ Crystals. *Phys. Status Solidi B-Basic Solid State Phys.* **2009**, *246* (6), 1306–1312.

(56) Yi, L.; Jian, L.; Chun-Lei, W.; Wen-Bin, S.; Yuan-Hu, Z.; Ji-Chao, L.; Liang-Mo, M. Thermoelectric Properties of Sr 0.61 Ba 0.39 Nb 2 O 6− δ Ceramics in Different Oxygen-Reduction Conditions. *Chinese Phys. B* **2015**, *24* (4), 047201.

(57) Li, Y.; Liu, J.; Wang, Z.; Zhou, Y.; Wang, C.; Li, J.; Zhu, Y.; Li, M.; Mei, L. Effects of Fluorine Doping on Thermoelectric Properties of Sr 0.61 Ba 0.39 Nb 2 O 6 Ceramics. *Phys. Scr.* **2015**, *90* (2), 025801.

(58) Kshirsagar, S. H.; Tarale, A. N.; Jigajeni, S. R.; Salunkhe, D. J.; Kulkarni, S. B.; Joshi, P. B. Ferroelectric and Magnetodielectric Properties of Cobalt-Doped Sr (x) Ba1-X Nb2O6 Ceramics. *J.*

Electron. Mater. **2015**, *44* (7), 2321–2330.

(59) Fang, T.-T.; Chung, H.-Y.; Lee, C.-H. Defects, Structure Changes, and the Effect of Random Fields on the Displacement of Off-Center Ions in $Sr_{0.50}Ba_{0.50}Nb_2O_6$ Doped with Combinations of Ce and Cr. *J. Am. Ceram. Soc.* **2010**, *93* (8), 2339–2345.

(60) Kaczmarek, S. M.; Tsuboi, T.; Leniec, A.; Nakai, Y.; Leniec, G.; Berkowski, M.; Huang, W. Temperature Dependence of PL and EPR Spectra of $Sr_{0.33}Ba_{0.67}Nb_2O_6$: Cr (0.02 Mol%) Single Crystals. *J. Cryst. Growth* **2014**, *401*, 798–801.

(61) Ivleva, L. I.; Kozlova, N. S.; Zabelina, E. V. Study of the Temperature Dependence of the Electrical Conductivity in Strontium-Barium Niobate Crystals with Different Dopants. *Crystallogr. Rep.* **2007**, *52* (2), 328–331.

(62) Guzhakovskaya, K. P.; Burkhanov, A. I.; Ivleva, L. I.; Tumanov, I. E. The Behavior of Current and Dielectric Response in SBN-75:Cr Single Crystal under Illumination Effect. *Ferroelectrics* **2014**, *469* (1), 92–96.

(63) Olsen, G. H.; Selbach, S. M.; Grande, T. On the Energetics of Cation Ordering in Tungsten-Bronze-Type Oxides. *Phys. Chem. Chem. Phys.* **2015**, *17* (45), 30343–30351.

(64) El-Shazly, T. S.; Hassan, W. M. I.; Rahim, S. T. A.; Allam, N. K. Unravelling the Interplay of Dopant Concentration and Band Structure Engineering of Monoclinic Niobium Pentoxide: A Model Photoanode for Water Splitting. *Int. J. Hydrog. Energy* **2015**, *40* (40), 13867–13875.

(65) Ottini, R.; Tealdi, C.; Tomasi, C.; Tredici, I. G.; Soffientini, A.; Anselmi-Tamburini, U.; Ghigna, P.; Spinolo, G. Feasibility of Electron and Hole Injection in Heavily Doped Strontium Barium Niobate (SBN50) Sr0.5Ba0.5Nb2O6 for Thermoelectric Applications. *J. Appl. Phys. 121*, 085104.

(66) Maglia, F.; Dapiaggi, M.; Tredici, I.; Maroni, B.; Anselmi-Tamburini, U. Synthesis of Fully Dense Nanostabilized Undoped Tetragonal Zirconia. *J. Am. Ceram. Soc.* **2010**, *93* (7), 2092–2097.

(67) Lutterotti, L.; Matthies, S.; Wenk, H.-R. MAUD: A Friendly Java Program for Material Analysis Using Diffraction. *IUCr: Newsletter of the CPD* **1999**, *21*, 14–15.

(68) D'Acapito, F.; Colonna, S.; Pascarelli, S.; Antonioli, G.; Balerna, A.; Bazzini, A.; Boscherini, F.; Campolungo, F.; Chini, G.; Dalba, G.; et al. GILDA Italian Beamline on BM08. *ESRF Newsl.* **1998**, *30*, 42–44.

(69) Ravel, B.; Newville, M. ATHENA, ARTEMIS, HEPHAESTUS: Data Analysis for X-Ray Absorption Spectroscopy Using IFEFFIT. *J Synchrotron Rad, J Synchrotron Radiat* **2005**, *12* (4), 537–541.

(70) Binsted, N.; Hasnain, S. S. State-of-the-Art Analysis of Whole X-Ray Absorption Spectra. *J. Synchrot. Radiat.* **1996**, *3*, 185–196.

(71) Kolodiazhnyi, T.; Petric, A.; Niewczas, M.; Bridges, C.; Safa-Sefat, A.; Greedan, J. E. Thermoelectric Power, Hall Effect, and Mobility of N-Type BaTiO3. *Physical Review B 68 , 085205 ~ 2003 ! 68*, 085205.

(72) Cox, P. A. *Transition Metal Oxides: An Introduction to Their Electronic Structure and Properties*; Clarendon Press, Oxford, 1995.

(73) Atomistic Simulation Group, Materials Department of Imperial College. Database of Ionic Radii - http://abulafia.mt.ic.ac.uk/shannon/ptable.php (accessed May 12, 2016).